



Editor's Pick | Structural Biology | Full-Length Text

Architectural organization and *in situ* fusion protein structure of lymphocytic choriomeningitis virus

Joon S. Kang,^{1,2,3} Kang Zhou,¹ Hui Wang,^{1,3} Sijia Tang,⁴ Kristin Van Mouwerik Lyles,⁵ Ming Luo,^{5,6} Z. Hong Zhou^{1,2,3}**AUTHOR AFFILIATIONS** See affiliation list on p. 12.

ABSTRACT Arenaviruses exist globally and can cause hemorrhagic fever and neurological diseases, exemplified by the zoonotic pathogen lymphocytic choriomeningitis virus (LCMV). The structures of individual LCMV proteins or their fragments have been reported, but the architectural organization and the nucleocapsid assembly mechanism remain elusive. Importantly, the *in situ* structure of the arenavirus fusion protein complex (glycoprotein complex, GPC) as present on the virion prior to fusion, particularly with its integral stable signal peptide (SSP), has not been shown, hindering efforts such as structure-based vaccine design. Here, we have determined the *in situ* structure of LCMV proteins and their architectural organization in the virion by cryogenic electron tomography. The tomograms reveal the global distribution of GPC, matrix protein Z, and the contact points between the viral envelope and nucleocapsid. Subtomogram averaging yielded the *in situ* structure of the mature GPC with its transmembrane domain intact, revealing the GP2-SSP interface and the endodomain of GP2. The number of RNA-dependent RNA polymerase L molecules packaged within each virion varies, adding new perspectives to the infection mechanism. Together, these results delineate the structural organization of LCMV and offer new insights into its mechanism of LCMV maturation, egress, and cell entry.

IMPORTANCE The impact of COVID-19 on public health has highlighted the importance of understanding zoonotic pathogens. Lymphocytic choriomeningitis virus (LCMV) is a rodent-borne human pathogen that causes hemorrhagic fever. Herein, we describe the *in situ* structure of LCMV proteins and their architectural organization on the viral envelope and around the nucleocapsid. The virion structure reveals the distribution of the surface glycoprotein complex (GPC) and the contact points between the viral envelope and the underlying matrix protein, as well as the association with the nucleocapsid. The morphology and sizes of virions, as well as the number of RNA polymerase L inside each virion vary greatly, highlighting the fast-changing nature of LCMV. A comparison between the *in situ* GPC trimeric structure and prior ectodomain structures identifies the transmembrane and endo domains of GPC and key interactions among its subunits. The work provides new insights into LCMV assembly and informs future structure-guided vaccine design.

KEYWORDS arenavirus, lymphocytic choriomeningitis virus, cryogenic electron tomography, *in situ* structures, spike proteins, virion, prefusion

Lymphocytic choriomeningitis virus (LCMV), a rodent-borne human pathogen, is a member of the Arenaviridae family in the Bunyvirales order. Globally distributed by the dispersion of the rodent reservoir, LCMV is a widely used experimental model for viral pathogenesis studies (1, 2). Although typically asymptomatic in healthy individuals, LCMV infection poses a threat to immunosuppressed patients, children, and pregnant women. For example, LCMV can cause aseptic meningitis in immunocompromised

Editor Rebecca Ellis Dutch, University of Kentucky College of Medicine, Lexington, Kentucky, USA

Address correspondence to Z. Hong Zhou, Hong.Zhou@ucla.edu.

Joon S. Kang, Kang Zhou, and Hui Wang contributed equally to this article. Author order was determined by drawing straws.

The authors declare no conflict of interest.

See the funding table on p. 13.

Received 7 April 2024

Accepted 9 August 2024

Published 27 September 2024

Copyright © 2024 American Society for Microbiology. All Rights Reserved.

individuals, while prenatal infection can cause abortion or severe congenital disabilities (3, 4).

LCMV is a pleomorphic enveloped virus that contains segmented negative-strand RNA genomes with one large (L) segment of ~7.5 kb and one small (S) segment of ~3.5 kb. Each segment contains two open reading frames (ORFs) encoding two gene products in opposite orientations, allowing for the expression of early and late genes (5). The large segment encodes the large RNA-dependent RNA polymerase (RdRp) (L, 200 kDa) and the multi-functional matrix protein (Z, 11 kDa). The small segment encodes the viral nucleoprotein (NP, 63 kDa) and precursor glycoprotein complex (GPC, 75 kDa). Since its genomic RNA is negative sense, LCMV relies on the packaged RdRp for its genome replication. L and NP are produced first from mRNA as early products. These early gene products act on the viral gene to make the late gene products, Z and GPC. GPC is initially expressed as a single polypeptide near and translocated to the endoplasmic reticulum, where a stable signal peptide (SSP, aa 1–58) is cleaved from its N terminus by the host signal peptidase (6). Then, GPC is translocated to Golgi, where it is additionally cleaved by the host convertase subtilisin kexin isozyme 1 (SKI-1)/site 1 protease (S1P), yielding peripheral glycoprotein 1 (GP1, aa 59–265) and transmembrane glycoprotein 2 (GP2, aa 266–498). GP1 is responsible for receptor engagement (7–10), and GP2 is responsible for membrane fusion (11–13). LCMV GPC belongs to the class one viral fusion protein, which also includes GPCs of human immunodeficiency virus (HIV), Ebola virus, and severe acute respiratory syndrome coronavirus 2. Because these viruses are enveloped, they must fuse with the host membrane to release their genetic material through the fusion pore (6, 14).

When the class one fusion protein concludes its final translocation to the membrane, its stable signal peptide (SSP) is generally degraded and does not remain as part of the mature GPC (15). However, compared to other class one fusion proteins, the LCMV SSP remains associated with the mature GPC—a unique feature of arenaviruses. After its cleavage at the ER, SSP is myristoylated and rearranged to translocate its C-terminal tail to the cytosolic side of the membrane (16, 17). This allows SSP's interaction with GP2 and retention in the mature GPC (18). In addition to its conventional role in directing intracellular trafficking, arenavirus SSP is an integral third structural subunit, alongside GP1 and GP2, of mature GPC necessary for the proper maturation of GPC and pH-dependent fusion process (19–22). Arenavirus SSP is proposed to traverse the membrane twice, with two antiparallel transmembrane helices connected by an eight-amino acid ectodomain loop (23, 24), but the complete structure of mature GPC with SSP intact remains unknown (12, 25, 26).

To address this, we obtained a 3D density map of the whole virion using cryogenic electron tomography (cryoET) and the density map of the prefusion state of LCMV GPCs by conducting subtomogram averaging (STA). We reconstructed a 3D model of the mature GPC with its transmembrane region intact, which reveals the GP2-SSP interface and GP2 endodomain. We also used our whole virion tomogram to fit the previously resolved models of individual proteins (12, 25–35) to establish the architectural framework of the virion and unveil the interactions among GPC, Z, NP, and L proteins. Together, these findings provide a roadmap to understanding the structural organization of LCMV and its mechanism of maturation, egress, and cell entry.

RESULTS

Structural organization of the LCMV viral proteins

In the virion, large and small segments of the viral genome are encapsidated by NP in the nucleocapsids. Each nucleocapsid segment is associated with an L protein, and two nucleocapsid segments are co-packaged via interactions with membrane-associated Z proteins that also interact with GPs studded in the viral envelope. Structures of individual proteins from Arenavirus have been solved previously by X-ray crystallography and cryogenic electron microscopy (cryoEM) (12, 25–35). However, the architectural organization of these proteins in the virion and the assembly mechanism of NP and

RNA into the nucleocapsid are poorly understood. To address this, we used cryoET to reconstruct the 3D model of the LCMV virion at molecular resolution. The simultaneous reconstruction technique-like implementation was used to analyze the tomograms of virion particles (Fig. 1A). The tomograms were denoised and corrected for missing-wedge artifacts to improve the visualization of the low-resolution features (Fig. 1B). A virion of interest was segmented from the corrected tomogram to generate a complete map of a fully intact virion, revealing the external and internal structural organization (Fig. 1C and D). The external view features the pleomorphic viral envelope and the random distribution of GPs throughout the envelope. The fitting of the GP model (PDB 8DMI) suggests that our virion carries prefusion state GPCs (Fig. 1E). Internally, the nucleocapsid is mostly packed randomly, although the periphery forms a structured layer underneath the viral envelope. At the core, two L polymerases are wrapped around the surrounding components, likely to be nucleocapsids and genomic RNA (Fig. 1D).

Viral protein interactions were examined in detail by segmenting the virion map into regions of GP, viral envelope, nucleocapsids, and L polymerases. The most prominent type of interface was found between the viral envelope layer and the underlying nucleocapsid layer (Fig. 1E). These interfaces were displayed as small pieces of densities that bridge the two layers. These densities seem to provide anchorage for the nucleocapsids and the viral envelope, conferring structural rigidity to the nucleocapsids. To better discern these densities and that underneath, the viral envelope was removed, and previously resolved structure models were fitted into the remaining density (Fig. 1E and F). The Z monomers (PDB 5I72) were placed into the bridging density as dimension references. The density underneath the Z proteins was placed with the NP monomers (PDB 3T5N). The NP monomers directly contacting the viral envelope are spaced apart (~13 Å) and stacked in an organized manner (Fig. 1F and G). Moving away from the viral envelope, the nucleocapsids become less orderly and more packed.

Next, the potential interactions around L were examined more closely. To begin, two dense regions shown in the denoised tomogram were segmented, as they were proposed to represent the L polymerases. Based on the size and shape of these two dense regions, only L polymerases are large enough to occupy the space, other components such as NP, Z, and RNA are too small. (Fig. 1H). Then, the innermost layer surrounding the aforementioned segmented region was extracted, and the previously resolved L-Z complex (PDB 7X 6V) was fitted into the segmented region (Fig. 1I). The first interesting finding is that both dense regions are larger than the L-Z complex, indicating that the region contains additional proteins that may be associated with the L-Z complex. Another finding is that there are empty spaces between the core complex and the nucleocapsid layer around the core complex (Fig. 1H and I). While there exists an empty space between the core complex and the nucleocapsid, there are also contacts between the two structures, locking the core complex in place.

While examining the anchorages earlier in Fig. 1, we discovered a large number of distributed overlaps between the NP-membrane contact points and the GPC locations. To examine this relationship further, we first identified all contact points between the viral envelope and the nucleocapsid with the surface markers and moved the markers up along their longitudinal axis to the outer surface layer (Fig. 2A). Then, the contact point markers that coincided with GPCs were distinguished from those that did not (Fig. 2A and B). The GPCs coinciding with the contact point markers were further distinguished from those that did not (Fig. 2A and B). The total contact points were 180, of which 108 (60%) coincided with GPCs (Fig. 2C). The total GPCs were 135, of which 108 (80%) coincided with the contact points (Fig. 2D). These findings suggest that more than half of the contact points are found directly underneath GPCs and that GPCs are closely associated with the Z proteins, which serve as the anchorage of the nucleocapsid to the viral envelope.

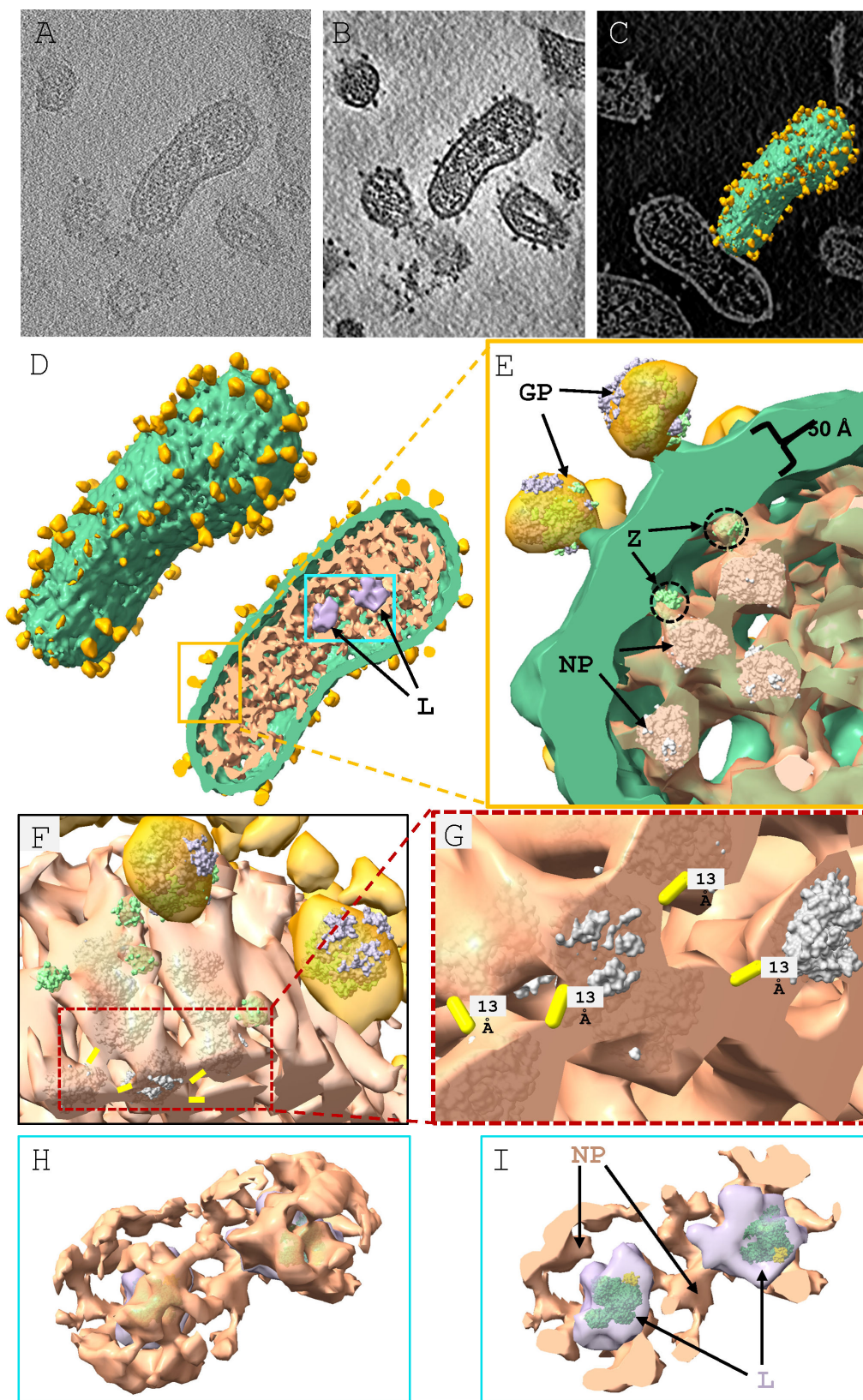


FIG 1 Architectural organization of LCMV: GP-Z-NP interface and peripheral NP arrangement. (A) XY density slice view of a cryoET tomogram containing a virion of interest. (B) XY slice view of the tomogram from panel A after deconvolution and (Continued on next page)

Fig 1 (Continued)

missing wedge correction. (C) Slice view of panel B with the segmented virion of interest. (D) Left: segmentation map of the virion from panel C. Right: cut-open view of the virion. (E) Zoom-in view of the yellow box region in panel D. Gold, glycoprotein; green, viral envelope; peach, nucleocapsid; and purple, L. The structures of GP (8DMI), Z (5I72), and NP (3T5N) were fitted or placed into the density as references. (F) Slightly rotated along the X-axis view of panel E with the viral envelope hidden. (G) Zoom-in view of the dotted red box region in panel F with the distance between the NPs indicated in yellow. (H and I) Segmentation of L with surrounding NP structures, where panel I is a sectional view of panel H.

In situ structure of LCMV GPC

The prefusion state GPC of LCMV is a trimer with each monomer subunit existing as a tripartite complex that consists of GP1, GP2, and SSP. Arenavirus SSP is an integral structural subunit of GPC that is necessary for the proper maturation and pH-dependent fusion process of GPC. Retention of arenavirus SSP is proposed to be achieved via the interaction of SSP with the C-terminal region of GP2. Structurally, arenavirus SSP is modeled to comprise two antiparallel transmembrane helices connected by an eight-amino acid ectodomain loop. Despite these findings, the available GPC-related structures of LCMV are the prefusion state GPC trimer structure, with each monomer consisting of GP1 and GP2 ectodomain, and the postfusion state GPC trimer structure, with each monomer consisting of GP2 ectodomain. Previous preparations were achievable by removing the hydrophobic domains, such as the GP2 TM domain and SSP domain (12, 25, 26).

CryoET, on the other hand, can be used to resolve structural features in the native environment, namely within the cell, by incorporating a subtomogram averaging approach. In STA, structures present in multiple copies, i.e., isotropic structures within the tomograms, can be extracted (subtomograms), aligned, and averaged, thus improving the signal-to-noise ratio and resolution. By taking advantage of STA, we resolved the *in situ* structure of membrane-bound LCMV GPC. GPCs of each virion were extracted as individually boxed particles from the earlier reconstructed tomograms. The box size was set to contain only one GPC and its underlying viral bilayer envelope. The GPC particles were subjected to RELION classification and refinements. RELION classification was set to generate four different classes, of which one class (5,835 particles, 16.7% of the extracted particles, data not shown) displayed the GPC ectodomain with the viral bilayer envelope underneath. The particles in this class were selected for the subsequent rounds of refinement, generating a final C3 symmetrized reconstruction with a 12-Å resolution (Fig. 3A). The ectodomain fitted well with the previously resolved model (PDB 8DMI), the prefusion state GPC (Fig. 3A). The map was sliced halfway along the z-axis to examine the internal density more closely (Fig. 3C). The thickness of the bilayer was 50 Å, matching the membrane thickness measured earlier on the segmentation map (Fig. 1D) and indicating that the two layers represent the leaflets of the phospholipid bilayer (Fig. 3C). Regarding the small density directly underneath the bottom leaflet, the C3 symmetrized Z monomers (PDB 5I72) fitted well into this region, corroborating our earlier findings of the distributed overlaps between GPC and Z (Fig. 3B, C, and G).

Next, the full-length LCMV GPC sequence was used to generate an AlphaFold2 (36) predicted model, which was utilized to build the TM domain and the C-terminal domain of GP2 (Fig. 3B). For the most part, there was no significant deviation in our GP2 model from that of PDB 8DMI (Fig. 3D). However, a deviation was observed in the region between F405 and I426 (Fig. 3E). While 8DMI modeled this entire region as an ectodomain helix, AlphaFold2 modeled the region from F405 to E412 as a flexible string, lengthening the region by ~16 Å, and the remainder as a helix (Fig. 3E). The lengthening of the region between F405 and E412 allowed us to bend this region to fit it into the narrow channel that connects the ectodomain and the top leaflet (Fig. 3D and E). In this way, the string penetrates into the top leaflet, and the subsequent region from A413 to I426 becomes the first TM helix domain that spans the top leaflet (Fig. 3C and E). The remaining helix domain extends perpendicular to the bilayer and crosses the central

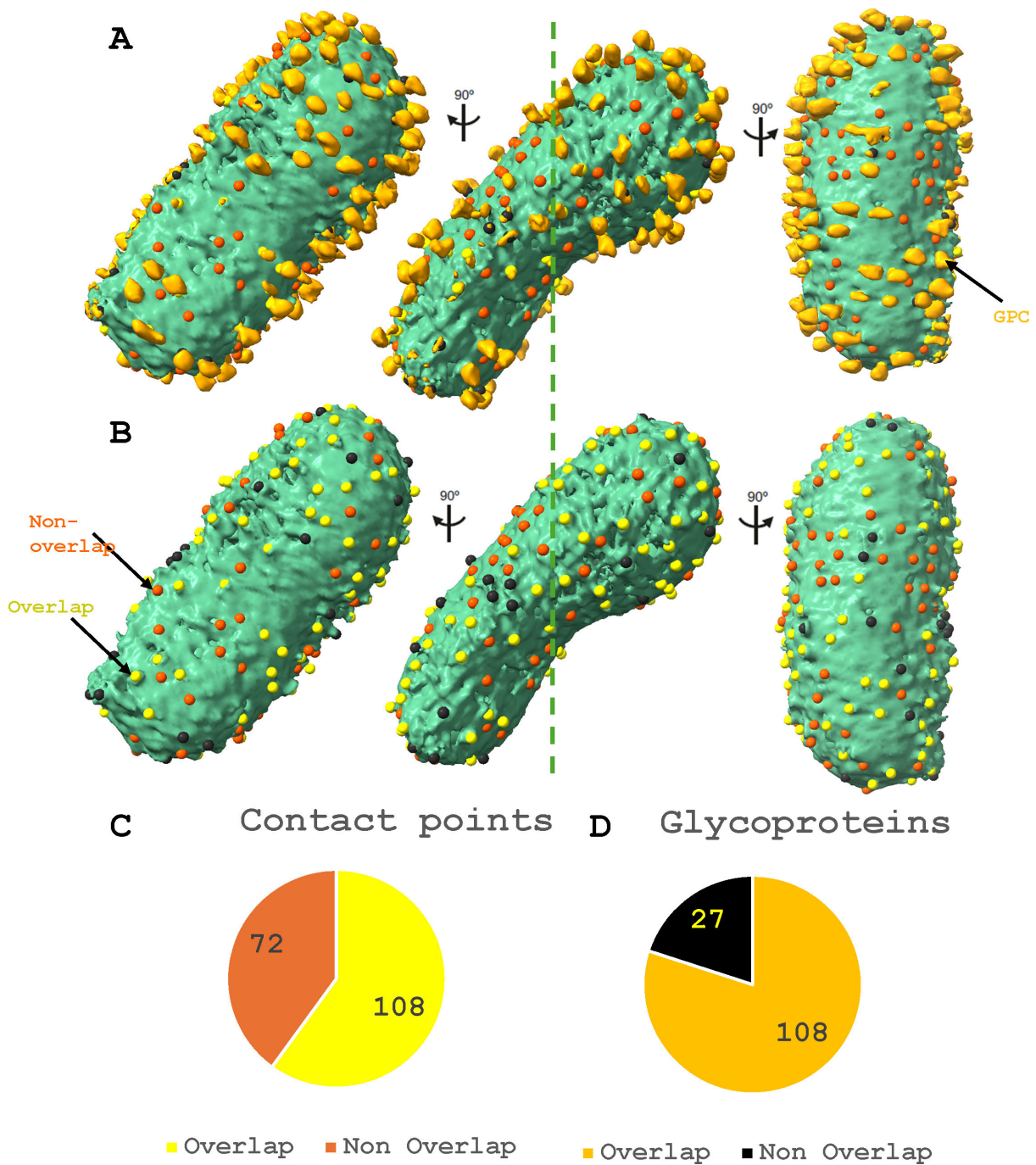


FIG 2 Distribution of contact points and how it relates to the glycoprotein. (A and B) Center: segmentation map of a virion from Fig. 1D with the distribution of contact points between the nucleocapsid and the membrane shown as surface markers. Yellow markers indicate the contact points that coincide with the GPCs. Orange markers indicate the contact points that do not coincide with the GPCs. Black markers indicate GPCs that do not coincide with the contact points. Left and right: the view rotated 90° along the axis indicated on the center view. (B) Segmentation map of a virion from panel A with GPCs hidden to show the yellow surface markers among others, which indicate the overlap between the contact points and GPC. (C) Pie chart depicting the distribution of nucleocapsid-membrane contact points that do/do not coincide with the GPs. (D) Pie chart depicting the distribution of GPs that do/do not coincide with the nucleocapsid-membrane contact points. The color code follows the marker color code in panels A and B.

density between the bilayers (Fig. 3C). A kink is introduced in the middle of the TM helix due to the cyclic P433 (Fig. 3C and F). The second TM helix extends from L436 to L453, spanning the bottom leaflet of the bilayer. Following the TM domain, the cytoplasmic tail begins at K457, followed by the zinc-binding domains 1 and 2 (ZBD1 and 2) (Fig. 3G).

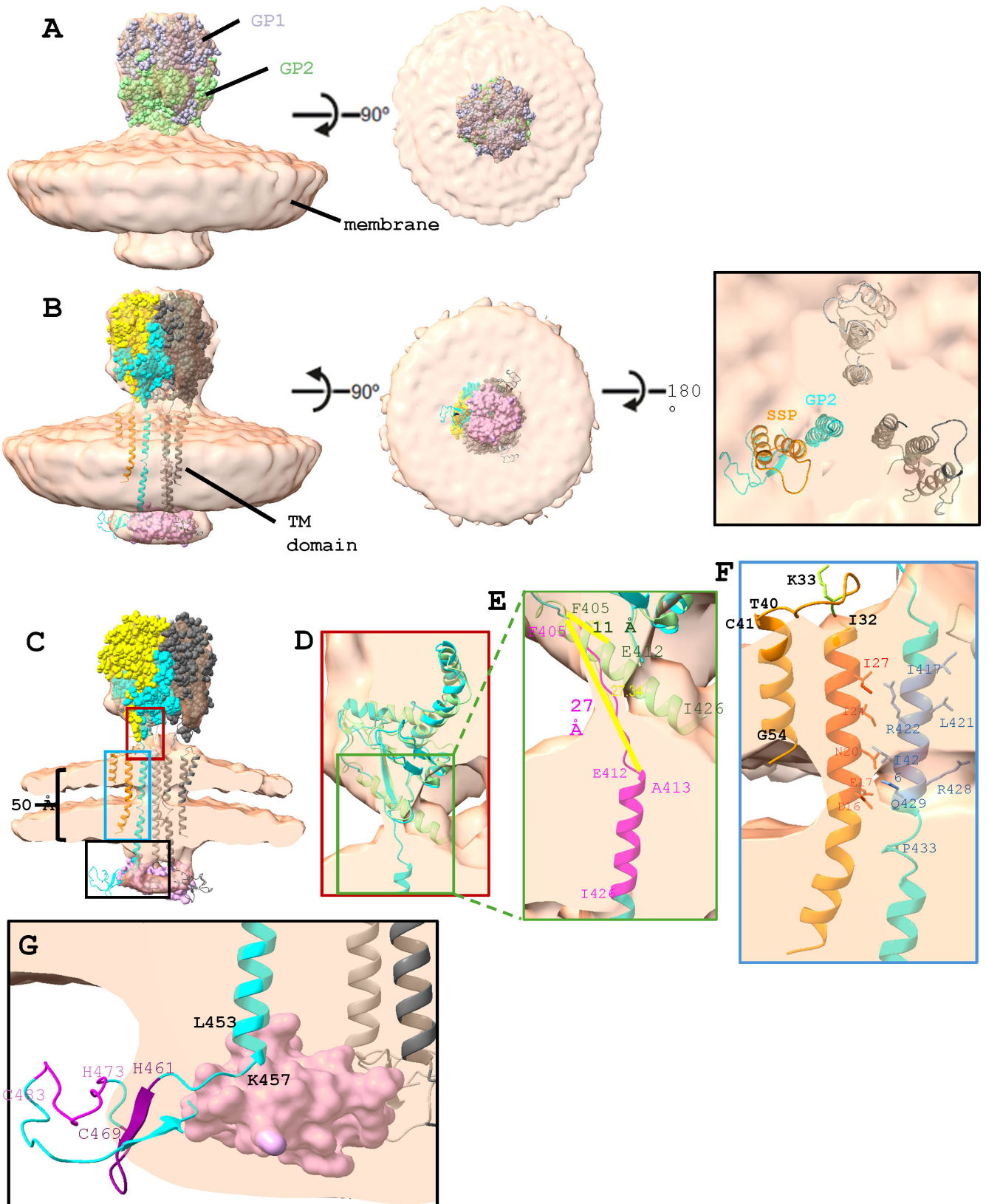


FIG 3 *In situ* structure of GPC using subtomogram averaging. (A) STA reconstruction (peach) fitted with 8DMI in space-filling model representation. GP1 is in gray, and GP2 is in light green (left, top view). (B) STA reconstruction fitted with our model and C3-symmetrized monomers of 5I72. GP1 is in yellow, GP2 is in cyan, SSP is in orange, and the Z monomer is in pink. Other GPCs are in dark gray and light gray. Ectodomain in space-filling model representation, and TM (Continued on next page)

Fig 3 (Continued)

domain and C-terminal domain in cartoon representation (left, bottom view). (Right) Top view with the ectodomain removed. (C) Cut-open view of panel B. The threshold has been adjusted from panels A and B to better define the bilayer and the TM domain density. (D) Zoom-in view of the burgundy-boxed region in panel C. It shows the superimposition of 8DMI GP2 (light green) and our modeled GP2 domain (cyan). The models are in cartoon representation. (E) Zoom-in view of the green-boxed region in panel D. The region between F405 and I426 of our model is highlighted in magenta. The distance between F405 and E412 of both models is measured using the Chimera tape tool. (F) Zoom-in view of the blue-boxed region in panel C. The hydrophobic residues are labeled. SSP helix 1 residues that are potentially interacting with GP2 are highlighted in darker orange, and the GP2 residues that are interacting with SSP helix 1 and neighboring GP2 are colored in darker blue. Ectodomain and helix 2 residues of SSP are highlighted in orange. (G) Zoom-in view of the black boxed region in panel C. ZBD1 and 2 of GP2 are highlighted in dark purple and light purple, respectively. One Z monomer is displayed for clarity.

Next, the AlphaFold2 SSP model was utilized to complete the GPC modeling. The SSP model began with the helix 1 domain from G2 to I32, followed by an ectodomain from K33 to T40, and finished with the helix 2 domain from C41 to G54 (Fig. 3F). The longer helix 1, instead of the shorter helix 2, is positioned next to the GP2 helix as it better fits our density map (Fig. 3C). While the domain designation for the SSP ectodomain loop and helix 2 follows the previous finding, the helix 1 domain in our model deviates from the previous finding (6). Previously, the regions from G2 to T6 and from M7 to D16 were designated as the myristoylation motif and cytoplasmic loop, respectively. However, our model suggests that the aforementioned regions are part of helix 1 to accommodate the ~50 Å thick bilayer (Fig. 3C).

With the full GPC modeled, we next examined the model at the residue level to suggest potential interactions between SSP helix 1 and GP2 TM domain. Notwithstanding caution warranted for interpreting models based on cryoET structure of limited resolution, we propose residues D16, E17, N20, I24, and I27 of the SSP helix 1 domain and R422, I426, and Q429 of the GP2 TM domain as potential residues contributing to the two domain's TMs hydrophobic interaction as they point toward each other in our model (Fig. 3F). Residues I417, L421, and R428 of GP2 point toward the neighboring GP2, suggesting their potential role in inter-subunit interaction. Except for several hydrophilic residues, most residues involving interaction are hydrophobic. In summary, our model suggests that SSP retention is supported by the interaction between SSP helix 1 TM and GP2's TM helix domain.

Variation in the number of L polymerases packaged in LCMV

Arenaviruses have two segments of the RNA genome, large and small segments, each encoding two gene products. It has been assumed that each segment is encapsidated by polymeric NP subunits, and a nascent L polymerase is bound to the 3' and 5' ends of each segment, reminiscent of a pearl necklace with a pendant. This general description suggests that each virion contains two nucleocapsids and two nascent L polymerases. To better understand the nucleocapsid-polymerase relationship, we examined each virion in our reconstructed tomograms (Fig. 4A through D). Our 151 reconstructed tomograms contained 450 virions in total. The virions were grouped by the number of polymerases packaged, and the histogram was constructed (Fig. 4F). Interestingly, our findings revealed that not all virions were packaged with two polymerases (Fig. 4A through E). In fact, most virions were packaged with no polymerase, followed by those with one polymerase (Fig. 4F). Virions with two polymerases belonged to the third most abundant group. Many virions were packaged with more than two Ls, with one virion with up to 20 Ls. All virions had mature GPCs studded on their membranes, regardless of the number of Ls packaged.

To find out the relationship between the virion size and the number of polymerases packaged in the virion, we measured the diameter of the virions belonging to each group assigned in the histogram. For the pleomorphic virions, the long axis range was measured, as indicated in the figures (Fig. 4A and D). Virions with zero or one L were generally smaller than those with more Ls, but had the greatest size variation, ranging from 36 to 140 nm and 50 to 200 nm, respectively (Fig. 4G). Virions with 10 or more Ls

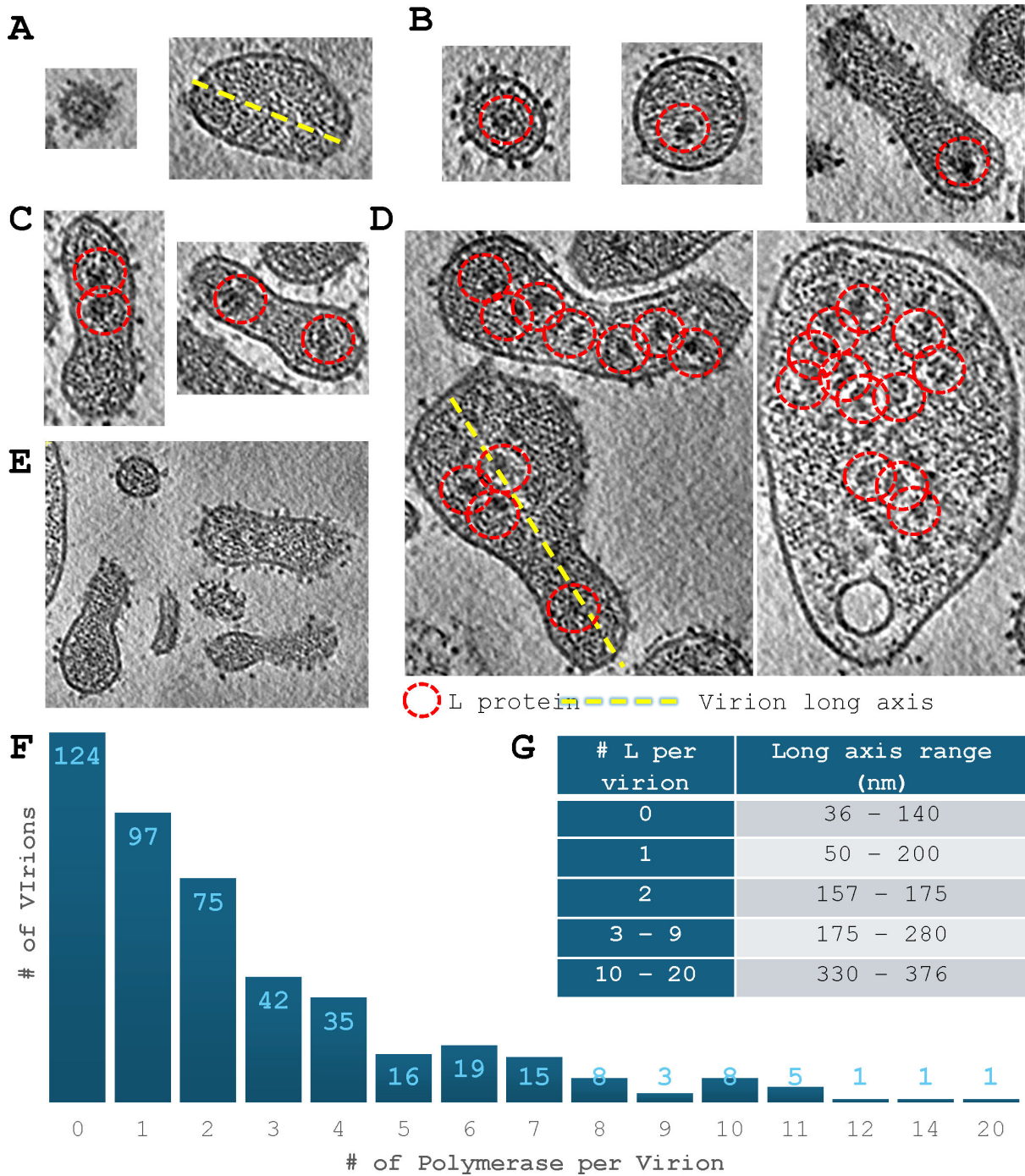


FIG 4 Denoised and missing-wedge corrected tomograms of LCMV virions packaged with different numbers of L. (A–E) XY slice view of denoised tomograms, highlighting virions with various sizes and numbers of polymerases. Red dashed circles indicate the polymerase complex. (A) Virions with 0 polymerase. (B) Virions with one polymerase. (C) Virions with two polymerases. (D) Virions with more than two polymerases. (E) Bird’s eye view of polymerase-packaged virions coexisting with other virions packaged with no polymerase. (F) Histogram of the number of virions versus the number of polymerases packaged in a virion. For example, there are 124 virions packaged with no polymerase. (G) Table showing the size variation of virion in relation to the number of polymerase(s) packaged in the virion. The long axis was measured as indicated in the dashed yellow line in panels A and D.

were some of the largest virions, ranging from 330 to 376 nm, which corresponds to a virion with 20 Ls (Fig. 4D, right). Virions with two Ls had the least size variation, ranging from 157 to 170 nm in diameter (Fig. 4C and G).

DISCUSSION

In this study, we have used cryoET and subtomogram averaging to determine the architectural organization and *in situ* protein structures of LCMV. Our cryoET reconstruction suggests that the contact points between Z proteins (30) and nucleocapsids (29) are randomly distributed, while Z proteins are associated with GPCs, whose distribution on the envelope also lacks order, and there is only partial overlap between these two distributions (Fig. 2). These findings agree with previous results on the subcellular co-localization and molecular interactions between Z and GPC (37). We suggest that Z have at least two roles: first, Z bridges between GPC and the nucleocapsid, thus anchoring the nucleocapsid to the envelope; second, the myristoylation of the N-terminal glycine of Z facilitates Z's interaction between the hydrophobic regions of GP and the envelope membrane (38). Inside the virion, N, the genomic RNA, and L together form the nucleocapsid. This way, the association among GPC (26), envelope membrane, Z (30), nucleocapsid (29), and L (39) defines the structural integrity and shape of LCMV. These suggestions await testing by future high-resolution structures.

Our STA of GPC and modeling suggest that the retention of SSP is mainly achieved via hydrophobic interactions between the TM domain of GP2 and the helix 1 domain of SSP. The model supports the findings from the screening assay that identified residues 434–437 of the GP2 TM domain and residues 25–27 of SSP helix 1 as the main residues targeted by the inhibitors, suggesting their critical roles in stabilizing the GP2-SSP interface (22, 40–43). In addition, the extracellular exposure and GP2 proximity of residue K33 of the ectodomain loop of SSP in our model allow for pH sensing and fit well with previous finding of the role of the highly conserved K33 on the pH-dependent fusion activity of GPC (22). At the same time, our model also reveals new findings. First, a 50-Å thick native membrane bilayer was observed, indicating that the TM should be longer than previously predicted based only on sequence (6). This observation has necessitated modeling residues 16–24 and residues 417–429 as part of TMs in SSP and GP2, respectively. Second, our model suggests that the previously identified ectodomain helix of GP2 (F405–I426) may instead be the first helix of the TM domain and that the first half of this helix has to be a flexible, lengthened loop so that the rest of the structure can span the bilayer. Without the bending and the extra length, the ZBD1 and ZBD2 domains would become part of the TM domain instead of the cytosolic domains. The deviation may have arisen due to the absence of the C-terminal domain and the different sample preparation methods in the previous structure study (26). Third, our model suggests that the previously identified 20 AA-long region of GP2 between positions 428 and 447 (26) can only span one leaflet of the bilayer. This leads to the second finding regarding the proposed interaction between the GP2 ZBD2 domain and the C-terminal end of SSP. While it is speculated that the conserved C57 of the SSP C-terminus may function as the fourth ligand of the tetrahedral coordination of zinc in the cytoplasmic ZBD2 domain of GP2 (18), that model seems unlikely as the SSP helix 2 can only span the top leaflet of the ~50-Å thick bilayer. Taken together, our model suggests infeasibility of the interaction between the GP2 ZBD2 domain and the C-terminal end of SSP. Our model does show an interaction between GP2 ZBD2 and a Z monomer, which may help explain our finding on the distributed overlaps between GPC and Z.

The large variation in the number of Ls packaged in the virion discovered by our cryoET analyses adds new perspectives to the infection mechanism of LCMV. First, the abundance of virions with various numbers of Ls but all with intact GPCs suggests that the egress of LCMV can occur at any point in time as long as the proper maturation and intracellular trafficking of the GPC is completed. With no strict requirement for packaging of the nucleocapsid-L complex, LCMV may lack strategic temporal regulation of its egress, such as lytic to lysogenic transition seen in HIV-1 (44). Second, the great abundance of virions with no or one L suggests that LCMV mainly relies on these types of virions for their survival. To overcome their lack of strategic egress regulation, LCMV may use degenerate virions to increase the probability of reassortment, which helps to evade the host immunity. In addition, virions with more than two Ls may be used as

special units for expedited viral transcription for the rapid expression of viral proteins upon host cell entry, achieving more efficient virion production. Third, an unrestricted strategy might be a preferred way for LCMV to evolve due to its simple architectural organization—other NSVs require more sophisticated assembly checking due to their complex structure (45). As a comparison, the influenza genome contains eight segments that encode 10 essential viral proteins and several strain-dependent accessory proteins (46, 47). Insofar as the polymerases are concerned, three of these segments encode for the subunits of the heterotrimeric polymerase of the influenza virus (48, 49). This suggests that if the segments were randomly packaged upon egress, there are 1 in 56 chances for influenza virus and 1 in 3 chances for LCMV for the proper polymerase assembly to produce infectious particles. If we consider all other viral components in the probability calculation, random packaging becomes more feasible in LCMV with its simpler structure.

Due to the limited resolution of our reconstructions, it is difficult to discern further details of the nucleocapsid arrangement, the packed complex around L, and the TM domain of GP2. Nonetheless, our cryoET reconstructions have allowed the first structural description of LCMV virion, a significant zoonotic virus that has the potential to cause pandemic infections among the human population. Integration of the *in situ* structures with previous atomic models of individual components has led to the delineation of critical contacts among different viral proteins.

MATERIALS AND METHODS

Preparation of LCMV

BHK-21 cells were maintained with EMEM (ATCC), supplemented with 10% fetal bovine serum, at 37°C and 5% CO₂. At 90% confluency, LCMV inoculum diluted in EMEM with 1% fetal bovine serum was absorbed to BHK-21 cells for 1 hour, and the infected cells were maintained in EMEM, supplemented with 10% fetal bovine serum for 48 hours at 37°C and 5% CO₂. The supernatant was collected and clarified by centrifugation. LCMV was pelleted by centrifugation at 30,000 *g* for 2.5 hours at 4°C. The virus in the pellet was resuspended in phosphate-buffered saline (PBS) and further purified by sucrose gradient centrifugation (20%–50%) at 31,200 rpm in Beckman SW 41 Ti rotor for 1.5 hours at 4°C. The virus band was collected and concentrated in PBS. Purified LCMV was deactivated by UV radiation 30 min before use.

Grid preparation for cryoET

The purified, deactivated LCMV sample was diluted 100-fold in PBS, ultracentrifuged for 1 hour at 100,000 × *g*, and decanted to remove sucrose. The viral pellet was air-dried overnight in a cold room to be loosened and resuspended in 50 μL PBS. In preparation for the cryoEM, we added a 10 nm gold bead solution to the sample in a 1:20 volume ratio. The sample was applied to the carbon side of 200 mesh Cu Quantifoil 100 holey carbon films (R 3.5/1), which were glow discharged by Gatan Plasma System SOLARUS beforehand. The grids were loaded onto the manual plunger, blotted with the filter paper for 5 seconds, and plunged into liquid ethane/propane. Grids were stored in liquid nitrogen.

CryoET data collection and drift correction

The initial sample quality assessment was conducted using negative stain EM with 2% phosphate tungsten pH 7.5 on the FEI Tecnai TF20 at 200 kV equipped with a Gatan K2 direct electron detection camera. The final imaging was conducted with a Titan Krios electron microscope (Thermo Fisher Scientific) equipped with a Gatan imaging filter (GIF), and images were recorded on a post-GIF Gatan K3 direct electron camera operated in super-resolution electron-counting mode. The magnification was 53,000×, with a pixel size of 1.69 Å/pixel at the specimen level. Data collection was facilitated by SerialEM (50).

Tomographic tilt series were collected between -60° and 60° with a 3° angular increment in the dose-symmetry scheme (51). The total dose of each tilt series was $121 \text{ e}^-/\text{\AA}^2$. Tilt series movies were recorded in dose-fraction mode and binned two times with the graphics processing unit-accelerated program MotionCor2 (52) to generate a micrograph in a tilt series.

Tomogram reconstruction and segmentation

One hundred fifty-two tilt series were collected and reconstructed following the standard protocol provided by IMOD (53). The final tomograms were binned to a pixel size of 13.52 \AA , deconvoluted, and corrected for the missing-wedge artifacts with IsoNet (54) using defocus values estimated by CTFFIND4 (55). The corrected tomogram was segmented using plane/surface markers and the split map function in ChimeraX (56).

Glycoprotein particle picking, subtomogram averaging, and TM domain modeling

The corrected tomograms were used to pick the GP particles. In total, 1,568 particles were manually picked from four tomograms and used to train a neural network model for automatic picking using the "AI Autopicking" tool in TomoNet (57). In total, 34,775 particles were picked from 151 tomograms. The coordinates and orientations of these particles were formatted and imported to RELION 4 (58) for further refinement. In RELION, the imported subtomograms binned to a pixel size of 6.76 \AA were subjected to two rounds of "3D auto-refine." The refined subtomograms were binned to a pixel size of 3.38 \AA and underwent one round of "3D classification," from which a class containing 5,835 particles was selected for the subsequent two rounds of "3D auto-refine." The finalized C3-symmetrized reconstruction reported a 12-\AA resolution, which is based on the gold standard refinement procedures and the 0.143 Fourier shell correlation criterion. TM domain modeling was conducted using AlphaFold2 (36) and Coot (59). The full sequence of LCMV GPC was used to generate a model that was modified manually to fit our density map while minimizing the steric clash.

ACKNOWLEDGMENTS

We thank Lenka Milojević for assistance in map segmentation.

This project is supported by grants from the US NIH (R01AI171426 to M.L. and GM071940 to Z.H.Z.). We acknowledge the use of resources at the Electron Imaging Center for Nanomachines supported by UCLA and grants from the NIH (1S10OD018111) and the NSF (DBI-1338135 and DMR-1548924).

Z.H.Z. and M.L. conceptualized the study. Z.H.Z., K.Z., H.W., S.T., K.V.M.L., and M.L. designed the methodology. J.S.K., K.Z., H.W., Z.H.Z., and M.L. performed investigation and modeling. Z.H.Z. and M.L. supervised the study. J.S.K. and Z.H.Z. wrote the original draft. J.S.K., Z.H.Z., K.Z., H.W., and M.L. reviewed and edited the manuscript.

AUTHOR AFFILIATIONS

¹California NanoSystems Institute, University of California, Los Angeles, California, USA

²Molecular Biology Institute, University of California, Los Angeles, California, USA

³Department of Microbiology, Immunology and Molecular Genetics, University of California, Los Angeles, California, USA

⁴Institute of Biomedical Sciences, Georgia State University, Atlanta, Georgia, USA

⁵Department of Chemistry, Georgia State University, Atlanta, Georgia, USA

⁶Center for Diagnostics and Therapeutics, Georgia State University, Atlanta, Georgia, USA

AUTHOR ORCIDs

Joon S. Kang  <http://orcid.org/0000-0003-0818-0811>

Kang Zhou  <http://orcid.org/0000-0002-3034-2808>

Hui Wang  <http://orcid.org/0000-0002-9922-7170>

Kristin Van Mouwerik Lyles  <http://orcid.org/0000-0003-0395-673X>

Z. Hong Zhou  <http://orcid.org/0000-0002-8373-4717>

FUNDING

Funder	Grant(s)	Author(s)
HHS National Institutes of Health (NIH)	R01AI171426	Ming Luo
HHS National Institutes of Health (NIH)	R01GM071940	Z. Hong Zhou
HHS National Institutes of Health (NIH)	S10OD018111	Z. Hong Zhou

DATA AVAILABILITY

CryoET tomograms have been deposited in the Electron Microscopy Data Bank under accession numbers [EMD-46040](https://www.ebi.ac.uk/emdb/EMD-46040) (raw tomogram of LCMV virions) and [EMD-46039](https://www.ebi.ac.uk/emdb/EMD-46039) (sub-tomogram average for GPC). The data that support this study are available from the corresponding author upon reasonable request.

REFERENCES

- Albariño CG, Palacios G, Khristova ML, Erickson BR, Carroll SA, Comer JA, Hui J, Briese T, St George K, Ksiazek TG, Lipkin WI, Nichol ST. 2010. High diversity and ancient common ancestry of lymphocytic choriomeningitis virus. *Emerg Infect Dis* 16:1093–1100. <https://doi.org/10.3201/eid1607.091902>
- Oldstone MBA. 2007. A suspenseful game of “hide and seek” between virus and host. *Nat Immunol* 8:325–327. <https://doi.org/10.1038/ni0407-325>
- Jamieson DJ, Kourtis AP, Bell M, Rasmussen SA. 2006. Lymphocytic choriomeningitis virus: an emerging obstetric pathogen? *Am J Obstet Gynecol* 194:1532–1536. <https://doi.org/10.1016/j.ajog.2005.11.040>
- Meritet JF, Krivine A, Lewin F, Poissonnier MH, Poizat R, Loget P, Rozenberg F, Lebon P. 2009. A case of congenital lymphocytic choriomeningitis virus (LCMV) infection revealed by hydrops fetalis. *Prenat Diagn* 29:626–627. <https://doi.org/10.1002/pd.2240>
- Hallam SJ, Koma T, Maruyama J, Paessler S. 2018. Review of mammarenavirus biology and replication. *Front Microbiol* 9:1751. <https://doi.org/10.3389/fmicb.2018.01751>
- Pennington HN, Lee J. 2022. Lassa virus glycoprotein complex review: insights into its unique fusion machinery. *Biosci Rep* 42:BSR20211930. <https://doi.org/10.1042/BSR20211930>
- Cao W, Henry MD, Borrow P, Yamada H, Elder JH, Ravkov EV, Nichol ST, Compans RW, Campbell KP, Oldstone MB. 1998. Identification of alpha-dystroglycan as a receptor for lymphocytic choriomeningitis virus and Lassa fever virus. *Science* 282:2079–2081. <https://doi.org/10.1126/science.282.5396.2079>
- Smelt SC, Borrow P, Kunz S, Cao W, Tishon A, Lewicki H, Campbell KP, Oldstone MB. 2001. Differences in affinity of binding of lymphocytic choriomeningitis virus strains to the cellular receptor alpha-dystroglycan correlate with viral tropism and disease kinetics. *J Virol* 75:448–457. <https://doi.org/10.1128/JVI.75.1.448-457.2001>
- Sullivan BM, Emonet SF, Welch MJ, Lee AM, Campbell KP, de la Torre JC, Oldstone MB. 2011. Point mutation in the glycoprotein of lymphocytic choriomeningitis virus is necessary for receptor binding, dendritic cell infection, and long-term persistence. *Proc Natl Acad Sci U S A* 108:2969–2974. <https://doi.org/10.1073/pnas.1019304108>
- Teng MN, Borrow P, Oldstone MB, de la Torre JC. 1996. A single amino acid change in the glycoprotein of lymphocytic choriomeningitis virus is associated with the ability to cause growth hormone deficiency syndrome. *J Virol* 70:8438–8443. <https://doi.org/10.1128/JVI.70.12.8438-8443.1996>
- Eschli B, Quirin K, Wepf A, Weber J, Zinkernagel R, Hengartner H. 2006. Identification of an N-terminal trimeric coiled-coil core within arenavirus glycoprotein 2 permits assignment to class I viral fusion proteins. *J Virol* 80:5897–5907. <https://doi.org/10.1128/JVI.00008-06>
- Igonet S, Vaney MC, Vonrhein C, Bricogne G, Stura EA, Hengartner H, Eschli B, Rey FA. 2011. X-ray structure of the arenavirus glycoprotein GP2 in its postfusion hairpin conformation. *Proc Natl Acad Sci U S A* 108:19967–19972. <https://doi.org/10.1073/pnas.1108910108>
- York J, Agnihothram SS, Romanowski V, Nunberg JH. 2005. Genetic analysis of heptad-repeat regions in the G2 fusion subunit of the Junin arenavirus envelope glycoprotein. *Virology (Auckl)* 343:267–274. <https://doi.org/10.1016/j.virol.2005.08.030>
- Hughson FM. 1995. Structural characterization of viral fusion proteins. *Curr Biol* 5:265–274. [https://doi.org/10.1016/s0960-9822\(95\)00057-1](https://doi.org/10.1016/s0960-9822(95)00057-1)
- White JM, Delos SE, Brecher M, Schornberg K. 2008. Structures and mechanisms of viral membrane fusion proteins: multiple variations on a common theme. *Crit Rev Biochem Mol Biol* 43:189–219. <https://doi.org/10.1080/10409230802058320>
- Agnihothram SS, York J, Trahey M, Nunberg JH. 2007. Bitopic membrane topology of the stable signal peptide in the tripartite Junin virus GP-C envelope glycoprotein complex. *J Virol* 81:4331–4337. <https://doi.org/10.1128/JVI.02779-06>
- York J, Romanowski V, Lu M, Nunberg JH. 2004. The signal peptide of the Junin arenavirus envelope glycoprotein is myristoylated and forms an essential subunit of the mature G1-G2 complex. *J Virol* 78:10783–10792. <https://doi.org/10.1128/JVI.78.19.10783-10792.2004>
- Briknarová K, Thomas CJ, York J, Nunberg JH. 2011. Structure of a zinc-binding domain in the Junin virus envelope glycoprotein. *J Biol Chem* 286:1528–1536. <https://doi.org/10.1074/jbc.M110.166025>
- Burri DJ, Pasquato A, Ramos da Palma J, Igonet S, Oldstone MBA, Kunz S. 2013. The role of proteolytic processing and the stable signal peptide in expression of the Old World arenavirus envelope glycoprotein ectodomain. *Virology (Auckl)* 436:127–133. <https://doi.org/10.1016/j.virol.2012.10.038>
- Froeschke M, Basler M, Groettrup M, Dobberstein B. 2003. Long-lived signal peptide of lymphocytic choriomeningitis virus glycoprotein pGP-C. *J Biol Chem* 278:41914–41920. <https://doi.org/10.1074/jbc.M302343200>
- Shankar S, Whitby LR, Casquilho-Gray HE, York J, Boger DL, Nunberg JH. 2016. Small-molecule fusion inhibitors bind the pH-sensing stable signal peptide-GP2 subunit interface of the lassa virus envelope glycoprotein. *J Virol* 90:6799–6807. <https://doi.org/10.1128/JVI.00597-16>
- York J, Nunberg JH. 2009. Intersubunit interactions modulate pH-induced activation of membrane fusion by the Junin virus envelope glycoprotein GPC. *J Virol* 83:4121–4126. <https://doi.org/10.1128/JVI.02410-08>
- Messina EL, York J, Nunberg JH. 2012. Dissection of the role of the stable signal peptide of the arenavirus envelope glycoprotein in membrane fusion. *J Virol* 86:6138–6145. <https://doi.org/10.1128/JVI.07241-11>
- Saunders AA, Ting JPC, Meisner J, Neuman BW, Perez M, de la Torre JC, Buchmeier MJ. 2007. Mapping the landscape of the lymphocytic choriomeningitis virus stable signal peptide reveals novel functional domains. *J Virol* 81:5649–5657. <https://doi.org/10.1128/JVI.02759-06>

25. Hastie KM, Igonet S, Sullivan BM, Legrand P, Zandonatti MA, Robinson JE, Garry RF, Rey FA, Oldstone MB, Saphire EO. 2016. Crystal structure of the prefusion surface glycoprotein of the prototypic arenavirus LCMV. *Nat Struct Mol Biol* 23:513–521. <https://doi.org/10.1038/nsmb.3210>
26. Moon-Walker A, Zhang Z, Zyla DS, Buck TK, Li H, Diaz Avalos R, Schendel SL, Hastie KM, Crotty S, Saphire EO. 2023. Structural basis for antibody-mediated neutralization of lymphocytic choriomeningitis virus. *Cell Chem Biol* 30:403–411. <https://doi.org/10.1016/j.chembiol.2023.03.005>
27. Brunotte L, Kerber R, Shang W, Hauer F, Hass M, Gabriel M, Lelke M, Busch C, Stark H, Svergun DI, Betzel C, Perbandt M, Günther S. 2011. Structure of the Lassa virus nucleoprotein revealed by X-ray crystallography, small-angle X-ray scattering, and electron microscopy. *J Biol Chem* 286:38748–38756. <https://doi.org/10.1074/jbc.M111.278838>
28. Hastie KM, Cross RW, Harkins SS, Zandonatti MA, Koval AP, Heinrich ML, Rowland MM, Robinson JE, Geisbert TW, Garry RF, Branco LM, Saphire EO. 2019. Convergent structures illuminate features for germline antibody binding and pan-Lassa virus neutralization. *Cell* 178:1004–1015. <https://doi.org/10.1016/j.cell.2019.07.020>
29. Hastie KM, Liu T, Li S, King LB, Ngo N, Zandonatti MA, Woods VL, de la Torre JC, Saphire EO. 2011. Crystal structure of the Lassa virus nucleoprotein-RNA complex reveals a gating mechanism for RNA binding. *Proc Natl Acad Sci U S A* 108:19365–19370. <https://doi.org/10.1073/pnas.1108515108>
30. Hastie KM, Zandonatti M, Liu T, Li S, Woods VL, Saphire EO. 2016. Crystal structure of the oligomeric form of Lassa virus matrix protein Z. *J Virol* 90:4556–4562. <https://doi.org/10.1128/JVI.02896-15>
31. Li S, Sun Z, Pryce R, Parsy ML, Fehling SK, Schlie K, Siebert CA, Garten W, Bowden TA, Strecker T, Huisken JT. 2016. Acidic pH-induced conformations and LAMP1 binding of the Lassa virus glycoprotein spike. *PLoS Pathog* 12:e1005418. <https://doi.org/10.1371/journal.ppat.1005418>
32. Neuman BW, Adair BD, Burns JW, Milligan RA, Buchmeier MJ, Yeager M. 2005. Complementarity in the supramolecular design of arenaviruses and retroviruses revealed by electron cryomicroscopy and image analysis. *J Virol* 79:3822–3830. <https://doi.org/10.1128/JVI.79.6.3822-3830.2005>
33. Peng R, Xu X, Jing J, Wang M, Peng Q, Liu S, Wu Y, Bao X, Wang P, Qi J, Gao GF, Shi Y. 2020. Structural insight into arenavirus replication machinery. *Nature* 579:615–619. <https://doi.org/10.1038/s41586-020-2114-2>
34. Qi X, Lan S, Wang W, Schelde LM, Dong H, Wallat GD, Ly H, Liang Y, Dong C. 2010. Cap binding and immune evasion revealed by Lassa nucleoprotein structure. *Nature* 468:779–783. <https://doi.org/10.1038/nature09605>
35. Volpon L, Osborne MJ, Capul AA, de la Torre JC, Borden KLB. 2010. Structural characterization of the Z RING-eIF4E complex reveals a distinct mode of control for eIF4E. *Proc Natl Acad Sci U S A* 107:5441–5446. <https://doi.org/10.1073/pnas.0909877107>
36. Jumper J, Evans R, Pritzel A, Green T, Figurnov M, Ronneberger O, Tunyasuvunakool K, Bates R, Židek A, Potapenko A, et al. 2021. Highly accurate protein structure prediction with AlphaFold. *Nature* 596:583–589. <https://doi.org/10.1038/s41586-021-03819-2>
37. Capul AA, Perez M, Burke E, Kunz S, Buchmeier MJ, de la Torre JC. 2007. Arenavirus Z-glycoprotein association requires Z myristoylation but not functional RING or late domains. *J Virol* 81:9451–9460. <https://doi.org/10.1128/JVI.00499-07>
38. Perez M, Greenwald DL, de la Torre JC. 2004. Myristoylation of the RING finger Z protein is essential for arenavirus budding. *J Virol* 78:11443–11448. <https://doi.org/10.1128/JVI.78.20.11443-11448.2004>
39. Liu L, Wang P, Liu A, Zhang L, Yan L, Guo Y, Xiao G, Rao Z, Lou Z. 2023. Structure basis for allosteric regulation of lymphocytic choriomeningitis virus polymerase function by Z matrix protein. *Protein Cell* 14:703–707. <https://doi.org/10.1093/procel/pwad018>
40. Liu Y, Guo J, Cao J, Zhang G, Jia X, Wang P, Xiao G, Wang W. 2021. Screening of botanical drugs against Lassa virus entry. *J Virol* 95:e02429-20. <https://doi.org/10.1128/JVI.02429-20>
41. Tang K, Zhang X, Guo Y. 2020. Identification of the dietary supplement capsaicin as an inhibitor of Lassa virus entry. *Acta Pharm Sin B* 10:789–798. <https://doi.org/10.1016/j.apsb.2020.02.014>
42. York J, Nunberg JH. 2006. Role of the stable signal peptide of Junin arenavirus envelope glycoprotein in pH-dependent membrane fusion. *J Virol* 80:7775–7780. <https://doi.org/10.1128/JVI.00642-06>
43. Zhang X, Tang K, Guo Y. 2020. The antifungal isavuconazole inhibits the entry of lassa virus by targeting the stable signal peptide-GP2 subunit interface of lassa virus glycoprotein. *Antiviral Res* 174:104701. <https://doi.org/10.1016/j.antiviral.2019.104701>
44. Hokello J, Sharma AL, Dimri M, Tyagi M. 2019. Insights into the HIV latency and the role of cytokines. *Pathogens* 8:137. <https://doi.org/10.3390/pathogens8030137>
45. Zhou K, Si Z, Ge P, Tsao J, Luo M, Zhou ZH. 2022. Atomic model of vesicular stomatitis virus and mechanism of assembly. *Nat Commun* 13:5980. <https://doi.org/10.1038/s41467-022-33664-4>
46. Chen W, Calvo PA, Malide D, Gibbs J, Schubert U, Bacik I, Basta S, O'Neill R, Schickli J, Palese P, Henklein P, Bennink JR, Yewdell JW. 2001. A novel influenza A virus mitochondrial protein that induces cell death. *Nat Med* 7:1306–1312. <https://doi.org/10.1038/nm1201-1306>
47. Dou D, Revol R, Östbye H, Wang H, Daniels R. 2018. Influenza A virus cell entry, replication, virion assembly and movement. *Front Immunol* 9:1581. <https://doi.org/10.3389/fimmu.2018.01581>
48. Clifford M, Twigg J, Upton C. 2009. Evidence for a novel gene associated with human influenza A viruses. *J Virol* 6:198. <https://doi.org/10.1186/1743-422X-6-198>
49. Dey S, Mondal A. 2024. Unveiling the role of host kinases at different steps of influenza A virus life cycle. *J Virol* 98:e0119223. <https://doi.org/10.1128/jvi.01192-23>
50. Mastronarde DN. 2005. Automated electron microscope tomography using robust prediction of specimen movements. *J Struct Biol* 152:36–51. <https://doi.org/10.1016/j.jsb.2005.07.007>
51. Hagen WJH, Wan W, Briggs JAG. 2017. Implementation of a cryo-electron tomography tilt-scheme optimized for high resolution subtomogram averaging. *J Struct Biol* 197:191–198. <https://doi.org/10.1016/j.jsb.2016.06.007>
52. Zheng SQ, Palovcak E, Armache JP, Verba KA, Cheng Y, Agard DA. 2017. MotionCor2: anisotropic correction of beam-induced motion for improved cryo-electron microscopy. *Nat Methods* 14:331–332. <https://doi.org/10.1038/nmeth.4193>
53. Kremer JR, Mastronarde DN, McIntosh JR. 1996. Computer visualization of three-dimensional image data using IMOD. *J Struct Biol* 116:71–76. <https://doi.org/10.1006/jsbi.1996.0013>
54. Liu YT, Zhang H, Wang H, Tao CL, Bi GQ, Zhou ZH. 2022. Isotropic reconstruction for electron tomography with deep learning. *Nat Commun* 13:6482. <https://doi.org/10.1038/s41467-022-33957-8>
55. Rohou A, Grigorieff N. 2015. CTFIND4: fast and accurate defocus estimation from electron micrographs. *J Struct Biol* 192:216–221. <https://doi.org/10.1016/j.jsb.2015.08.008>
56. Pettersen EF, Goddard TD, Huang CC, Meng EC, Couch GS, Croll TI, Morris JH, Ferrin TE. 2021. UCSF ChimeraX: structure visualization for researchers, educators, and developers. *Protein Sci* 30:70–82. <https://doi.org/10.1002/pro.3943>
57. Wang H, Liao S, Yu X, Zhang J, Zhou ZH. 2024. TomoNet: a streamlined cryogenic electron tomography software pipeline with automatic particle picking on flexible lattices. *Biol Imaging* 4:e7. <https://doi.org/10.1017/S2633903X24000060>
58. Zivanov J, Otón J, Ke Z, von Kügelgen A, Pyle E, Qu K, Morado D, Castaño-Díez D, Zanetti G, Bharat TAM, Briggs JAG, Scheres SHW. 2022. A Bayesian approach to single-particle electron cryo-tomography in RELION-4.0. *Elife* 11:e83724. <https://doi.org/10.7554/eLife.83724>
59. Emsley P, Lohkamp B, Scott WG, Cowtan K. 2010. Features and development of Coot. *Acta Crystallogr D Biol Crystallogr* 66:486–501. <https://doi.org/10.1107/S0907444910007493>